The Astrophysical Journal Letters, 997:L2 (14pp), 2026 January 20 https://doi.org/10.3847/2041-8213/ae2f59

Circumplanetary Disk Candidate in the Disk of HD 163296 Traced by Localized Emission from Simple Organics

Andrés F. Izquierdo[1,8], Jaehan Bae[1], Maria Galloway-Sprietsma[1], Ewine F. van Dishoeck[2,3], Stefano Facchini[4], Giovanni Rosotti[4], Jochen Stadler[5], Myriam Benisty[6], and Leonardo Testi[7]
[1] Department of Astronomy, University of Florida, Gainesville, FL 32611, USA; andres.izquierdo.c@gmail.com
[2] Leiden Observatory, Leiden University, 2300 RA Leiden, The Netherlands
[3] Max-Planck Institut für Extraterrestrische Physik (MPE), Gießenbachstrasse 1, 85748, Garching bei München, Germany
[4] Dipartimento di Fisica, Università degli Studi di Milano, Via Celoria 16, 20133 Milano, Italy
[5] Université Côte d'Azur, Observatoire de la Côte d'Azur, CNRS, Laboratoire Lagrange, 06304 Nice, France
[6] Max-Planck Institute for Astronomy (MPIA), Königstuhl 17, 69117 Heidelberg, Germany
[7] Dipartimento di Fisica e Astronomia, Universitá di Bologna, I-40129 Bologna, Italy

Received 2025 September 12; revised 2025 November 5; accepted 2025 December 9; published 2026 January 14

Abstract

Atacama Large Millimeter/submillimeter Array observations suggest that the disk of HD 163296 is being actively shaped by embedded yet unseen protoplanets, as indicated by numerous gas and dust substructures consistent with planet–disk interaction models. We report the first detection of simple organic molecules, HCN and C_2H, tracing a candidate circumplanetary disk (CPD) in the HD 163296 system, located at an orbital radius of $R = 88 \quad 7$ au and azimuth $\phi = 46^\circ \quad 3^\circ$ (or $R = 0\farcs75$, PA $= 350^\circ$ in projected sky coordinates), and originating near the midplane of the circumstellar disk. The signature is localized but spectrally resolved, and it overlaps with a previously reported planet candidate, P94, identified through kinematic perturbations traced by CO lines. We propose a scenario in which the observed chemical anomalies arise from increased heating driven by the forming planet and ongoing accretion through its CPD, facilitating the thermal desorption of species that would otherwise remain frozen out in the disk midplane, and potentially triggering the activation barriers of chemical reactions that lead to enhanced molecular production. Based on a first-order dynamical analysis of the HCN spectrum from the CPD—isolated with a 7σ significance—we infer an upper limit on the planet mass of $1.8M_{\rm Jup}$, consistent with predictions from CO kinematics and constraints from direct imaging studies. By comparing the CPD sizes derived from our models with theoretical expectations where the CPD radius corresponds to roughly one-third of the planet's Hill radius, we favor CPD gas temperatures $T > 150$ K, planet masses $M_p < 1.0M_{\rm Jup}$, and CPD radii $R_{\rm CPD} < 2$ au.

Unified Astronomy Thesaurus concepts: Protoplanetary disks (1300); Astrochemistry (75); Planetary-disk interactions (2204); Exoplanet detection methods (489)

1. Introduction

The disk of HD 163296 has been identified as a promising host of ongoing planet formation, as evidenced by multiple annular signatures observed in both dust continuum and molecular line emission with the Atacama Large Millimeter/submillimeter Array (ALMA; I. de Gregorio-Monsalvo et al. 2013; A. Isella et al. 2016, 2018). Kinematic studies, also enabled by ALMA, further support a planetary origin for these features. Concentric deviations from Keplerian rotation around the dust substructures can be explained by invoking gap-carving, Jupiter-mass planets within the inner $R < 160$ au of the disk (R. Teague et al. 2018b), while in the outer regions large-scale velocity perturbations point to the possibility of an additional giant planet on a wide orbit ($R \sim 260$ au; C. Pinte et al. 2018b; J. Calcino et al. 2022).

More recently, A. F. Izquierdo et al. (2022, 2023) further investigated the kinematics of this system, detecting a strongly localized velocity perturbation traced by ^{12}CO and ^{13}CO $J = 2 \quad 1$ emission lines. Based on empirical comparisons with hydrodynamical models, the authors attributed this feature to a $1M_{\rm Jup}$ protoplanet (P94), located at the center of the perturbation, at an orbital radius of $R = 94 \quad 6$ au and an azimuth of $\phi = 50 \quad 3$ in disk-frame coordinates, corresponding to a projected separation of $R = 0\farcs77$ from the disk center and a position angle of PA $= 352\fdg1$, measured from north to east. The inferred mass of P94 is consistent with the nondetections at near-infrared wavelengths with Very Large Telescope/SPHERE (D. Mesa et al. 2019) and JWST/NIRCam (T. Uyama et al. 2025), which suggest upper limits of $\sim 4M_{\rm Jup}$ at this orbital separation, but remains sufficient to carve a dust and gas gap in the disk (R. Teague et al. 2018b).

Nevertheless, although crucial for indirect detection, CO lines are known to originate from intermediate to high altitudes above the midplane of this disk ($z/r \approx 0.15$–0.3; C. J. Law et al. 2021b; T. Paneque-Carreño et al. 2023; A. F. Izquierdo et al. 2023), making the derived planet mass model dependent—sensitive to assumptions about disk properties such as viscosity and vertical pressure structure (I. Rabago & Z. Zhu 2021)—and more susceptible to the influence of hydrodynamical instabilities than the midplane layers (M. Barraza-Alfaro et al. 2024).

Luckily, deep ALMA observations offer the opportunity to broaden our understanding of planet-driven signatures by probing a variety of molecular species that trace distinct radial and vertical regions of the disk, depending on their abundances

---

[8] NASA Hubble Fellowship Program Sagan Fellow.

and excitation conditions (see reviews by A. Miotello et al. 2023; K. I. Öberg et al. 2023). Of particular interest for planet searches are tracers of outflows and shock chemistry—such as SO, SiS, and SiO—some of which have recently been detected in disks near previously reported planet candidates (A. S. Booth et al. 2023; C. J. Law et al. 2023), as well as in disks with strong dynamical perturbations potentially driven by planets (F. Zagaria et al. 2025). Another important class of tracers accessible with ALMA includes molecules like HCN and C_2H, whose abundances are highly sensitive to high-temperature chemistry (A. M. S. Boonman et al. 2001; S. D. Doty et al. 2002; M. Agúndez et al. 2008), the strength of the ultraviolet (UV) radiation field (M. Agúndez et al. 2018; R. Visser et al. 2018), and the local C/O ratio (L. I. Cleeves et al. 2018). Consequently, thermochemical models predict that the gas-phase distribution of these molecules may be enhanced in the vicinity of giant planets owing to increased heating and UV irradiation associated with ongoing accretion onto the forming planet (L. I. Cleeves et al. 2015; Y. Aoyama et al. 2020; J. K. Calahan et al. 2023).

In this Letter, we present the first evidence for the presence of these simple organics in a circumplanetary region still embedded within its parent circumstellar disk (CSD). The system orbits the Herbig Ae star HD 163296, located at a distance of 101.5 pc from Earth at International Celestial Reference System equatorial coordinates $\alpha = 17^{\rm h}56^{\rm m}21\overset{\rm s}{.}$, $\delta = -21°57'21''$ (C. A. L. Bailer-Jones et al. 2018). The detected signatures manifest as localized intensity enhancements in HCN and C_2H lines, overlapping with the ^{12}CO and ^{13}CO velocity perturbations previously attributed to the kinematic planet candidate P94. Furthermore, these molecular anomalies appear to arise near the CSD midplane, suggesting an origin in the immediate vicinity of P94 and possibly tracing emission from a circumplanetary disk (CPD) around the planet.

CPDs are natural by-products of the planet formation process (S. Miki 1982; T. Tanigawa & S.-i. Watanabe 2002), yet observational evidence for them remains scarce, with detections reported in only two systems where the CSD material is already significantly depleted (A. Isella et al. 2019; M. Benisty et al. 2021; J. Bae et al. 2022). As a result, knowledge of key CPD properties such as temperature, size, and dynamical mass is also limited. In this work, we provide estimates of these parameters for the CPD candidate around P94 through a first-order analysis of the HCN line profile observed in its vicinity. These properties represent valuable proxies for the accretion dynamics and evolutionary stage of the protoplanet (J. Szulágyi et al. 2016; J. Szulágyi & C. Mordasini 2017; J. Fung et al. 2019) and are crucial for understanding the onset of satellite formation in the system (R. M. Canup & W. R. Ward 2002).

2. Observations and Disk Modeling

2.1. Datasets

The core of this work is based on archival ALMA data (Project ID: 2018.1.01055.L) targeting HCN in its rotational transition $J = 3$ 2, which is split into multiple hyperfine components. These data were originally reduced and analyzed by the MAPS collaboration (K. I. Öberg et al. 2021), which provides three fiducial, continuum-subtracted position–velocity cubes for this tracer, referred to as HF2, HF1, and HF3 (in order of ascending frequency), each centered on a different hyperfine transition within the group. HF2 and HF3 are centered on the faint peripheral $F = 3$ 3 and $F = 2$ 2 components, respectively, while HF1 is centered on the bright $F = 3$ 2 transition, at a rest frequency of $\nu = 265.886499$ GHz (H. S. P. Müller et al. 2001). At the channel spacing of the data, the $F = 3$ 2 line is blended with other bright components, $F = 2$ 1 and $F = 4$ 3. Under the assumption of local thermodynamic equilibrium, these lines account for ~92% of emission in the $J = 3$ 2 group (e.g., A. M. Mullins et al. 2016), and thus our analysis is dominated by their combined signal.

For the modeling of the HCN channel maps from both CSDs and CPDs we use the JvM-corrected HF3 cube, centered on the highest-frequency component at $\nu = 265.888522$ GHz, in which the localized intensity signal around the planet P94 was first identified. This choice, however, has no practical impact on the analysis, since all bright hyperfine components in the group are closely spaced in frequency and fall within the spectral coverage of any of the three fiducial cubes. Accordingly, the P94 intensity signal is also detected in the HF1 and HF2 cubes, both with and without JvM correction, as illustrated in Appendix B. We also use a fiducial datacube of C_2H emission provided by MAPS, focusing on the brightest transition, $F = 4$ 3 at $\nu = 262.004226$ GHz, in the hyperfine group $N = 3$ 2, $J = 7/2$ 5/2, where we identify spatial overlap with the localized HCN signal around P94. The synthesized beam size of all datasets used in this work is $0''.15 \times 0''.15$, and the velocity channels are spaced by 0.2 km s^{-1}, with rms noise levels of 0.43 mJy $beam^{-1}$ for HCN and 0.53 mJy $beam^{-1}$ for C_2H. Details of the data calibration and imaging procedures are provided in I. Czekala et al. (2021).

2.2. Model of the Disk HCN Intensity and Dynamics

The disk of HD 163296 exhibits significant substructure in HCN and C_2H emission, including annular enhancements at 48 and 114 au, a prominent dip at 79 au, and a central cavity in both cases (C. J. Law et al. 2021a), consistent with the similar formation pathways of these molecules (V. V. Guzmán et al. 2021). Figure 1 illustrates these annular features for HCN $J = 3$ 2, showing the absolute peak intensity map of the line alongside the Band 6 dust continuum, overlaid with the ^{12}CO Doppler-flip signature associated with the kinematic planet P94 (A. F. Izquierdo et al. 2022). We note that since the HCN peak intensity is dominated by emission from the CSD, the localized HCN signal associated with P94 is not visible in this map. Instead, it becomes apparent when the channel maps of the tracer are examined individually, as discussed in Section 3.2.

To model the channel-by-channel intensity and kinematics of the disk while capturing its radial substructures, we first ran DISCMINER to retrieve baseline geometric and line profile parameters assuming radially decreasing peak intensity and line width (see A. F. Izquierdo et al. 2025, for details), with the disk inclination fixed to the best-fit continuum value from J. Huang et al. (2018). In a second step, we fitted a customized version of the radial peak intensity, including two parametric Gaussian rings, while keeping all other parameters fixed. We restricted the

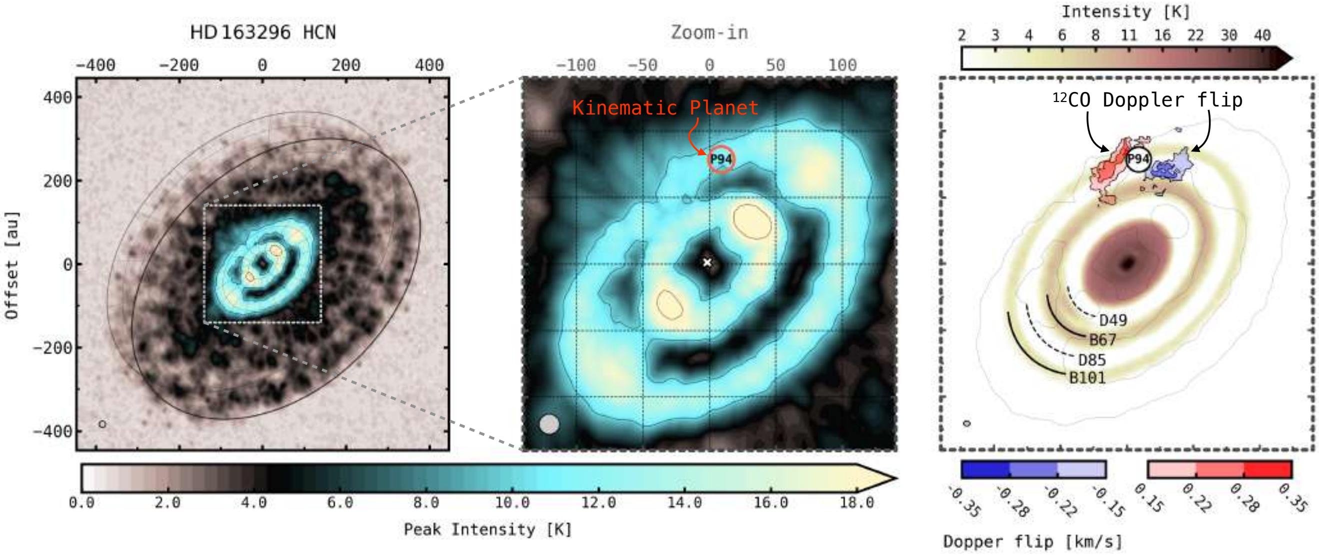

Figure 1. HCN and millimeter dust continuum emission from the disk of HD 163296 as observed with ALMA. The left panel shows the absolute peak intensity of HCN $J = 3 \rightarrow 2$ line data from the MAPS project (K. I. Öberg et al. 2021), computed using the Rayleigh–Jeans approximation, while the middle panel provides a zoomed-in view of the central region. For the same section, the right panel displays the millimeter dust continuum emission from DSHARP (S. M. Andrews et al. 2018; A. Isella et al. 2018), with dashed and solid lines marking the radial locations of selected continuum gaps (DXX) and rings (BXX), respectively. Overlaid is the localized ^{12}CO velocity perturbation identified by A. F. Izquierdo et al. (2022), along with contours of HCN emission at $T = 10$ K for reference. The circle labeled P94 marks the location of the planet candidate associated with this velocity feature, which we propose is also responsible for the localized intensity signals observed in the channel maps of HCN and C_2H lines (see Section 3.2).

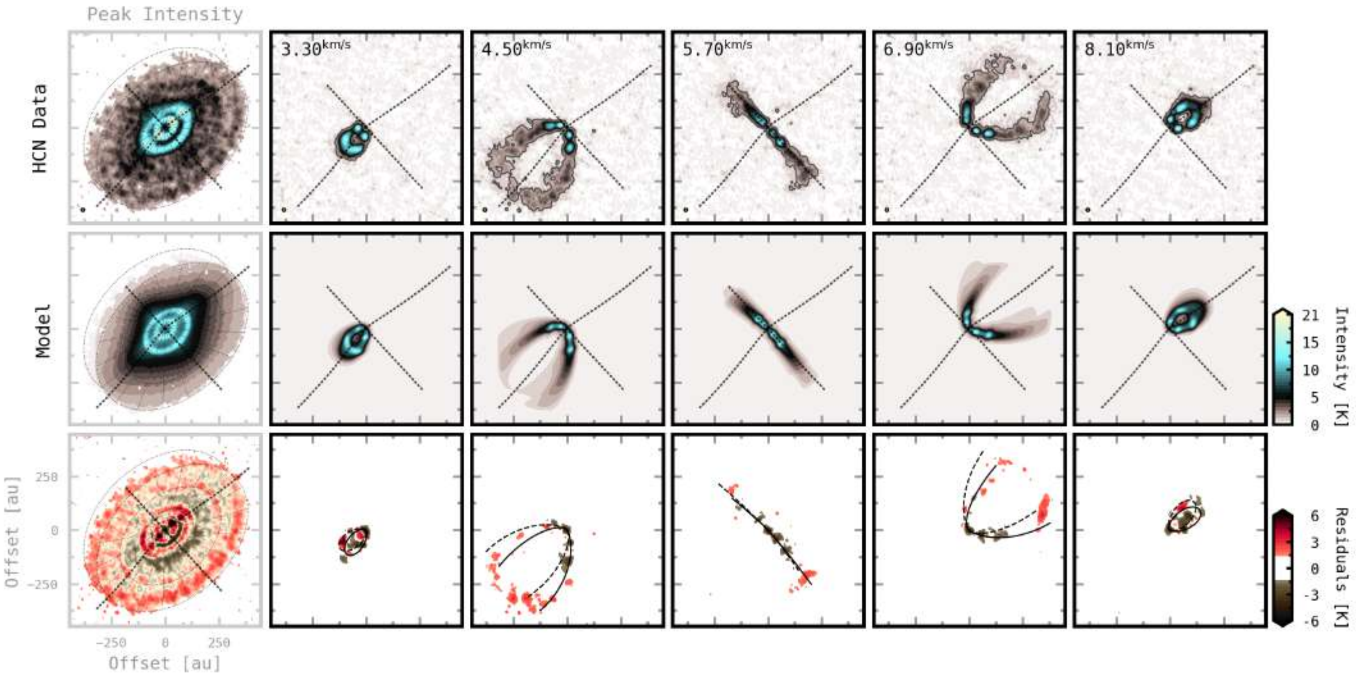

Figure 2. Selected channel maps of HCN line brightness temperature from the HD 163296 disk (top row), compared with those from the best-fit DISCMINER model (middle row), computed using the Rayleigh–Jeans approximation. Contours in the top row enclose emission above five times the rms noise level of 0.33 K. Also shown are intensity residuals for each velocity channel (bottom row), with overlaid isovelocity contours from the model upper and lower surfaces shown as solid and dashed lines, respectively. For reference, the best-fit systemic velocity is $\upsilon_{\rm sys} = 5.79$ km s^{-1}. The synthesized beam of the observations is shown in the lower left corner of the panels in the top row. Residuals with amplitudes lower than four times the rms noise have been masked.

modeling to the HCN data to avoid contamination from the strong hyperfine components present in C_2H. Table 1 summarizes the functional forms of the adopted model and the resulting best-fit parameters, and Figure 2 presents selected HCN intensity channel maps, together with the corresponding best-fit model and residuals.

Table 1
List of Attributes Adopted in Our DISCMINER Channel-map Model of the HCN $J = 3 \rightarrow 2$ Emission Line from the Disk of HD 163296, Along with the Corresponding Best-fit Parameters

Attribute	Prescription	Best-fit Parameters for HCN $J = 3 \rightarrow 2$
Orientation	uniform i, PA, x_c, y_c	$i = 46\overset{\circ}{.}7$ [Fixed] PA $= 312\overset{\circ}{.}8$ $x_c = -1.5$ mas $y_c = 32.0$ mas
Velocity	$\upsilon_{\rm k} = \sqrt{\frac{GM_\star}{r^3}}R$, $\upsilon_{\rm LSRK}$	$M_\star = 1.99\,M_\odot$ $\upsilon_{\rm LSRK} = 5.79$ km s^{-1}
Upper surface	$z = z_0(R/D_0)^p \exp[-(R/R_t)^q]$	$z_0 = 21.7$ au $p = 1.50$ $R_t = 429.7$ au $q = 1.03$
Lower surface	$z = -z_0(R/D_0)^p \exp[-(R/R_t)^q]$	$z_0 = 17.3$ au $p = 1.44$ $R_t = 456.5$ au $q = 0.77$
Peak intensity	$I_p(R \leqslant R_{\rm out}) = I_0(R/D_0)^p(z/D_0)^q$	$I_0 = 124.4$ mJy pixel^{-1} $p = -4.31$ $q = 3.04$ $R_{\rm out} = 405.7$ au
Line width	$L_w = L_{w0}(R/D_0)^p(z/D_0)^q$	$L_{w0} = 0.07$ km s^{-1} $p = 0.42$ $q = -1.07$
Line slope	$L_s = L_{s0}(R/D_0)^p$	$L_{s0} = 1.42$ $p = 0.24$
Intensity ring #1	$I_1 = B_1 \exp\left(-\frac{(R-\mu_1)^2}{2\sigma_1^2}\right)$	$B_1 = 1.5$ mJy pixel^{-1} $\mu_1 = 47.6$ au $\sigma_1 = 2.5$ au
Intensity ring #2	$I_2 = B_2 \exp\left(-\frac{(R-\mu_2)^2}{2\sigma_2^2}\right)$	$B_2 = 0.7$ mJy pixel^{-1} $\mu_2 = 114.3$ au $\sigma_1 = 7.3$ au

Note. G is the gravitational constant. $D_0 = 100$ au is a normalization factor. In disk coordinates, z denotes the emission height above the midplane, R the cylindrical radius, and r the spherical radius. The composite model peak intensity is given by $I_f = I_p + I_1 + I_2$ and is set to zero for radii beyond $R_{\rm out}$. The systemic velocity, $\upsilon_{\rm LSRK}$, was shifted by 2.36 km s^{-1} to align with the rest frequency of the reference $J = 3 \rightarrow 2$, $F = 3 \rightarrow 2$ transition.

3. Results

3.1. Radial and Vertical Distribution of HCN in the Circumstellar Disk

Modeling efforts on the chemical composition of protoplanetary disks suggest that HCN and C_2H are effective tracers of UV radiation, as they can be efficiently synthesized through UV-driven chemistry in warm gas (C. Walsh et al. 2012; M. Agúndez et al. 2018; R. Visser et al. 2018). These models also indicate that, in the outer and colder regions of disks, HCN is primarily found at intermediate heights ($z/R \approx 0.1-0.3$) above the midplane, where it likely forms via gas-phase chemistry involving ion–molecule reactions followed by dissociative recombination. More generally, the precise radial and vertical distributions of HCN and other such molecules sensitive to the UV radiation field depend strongly on the local UV opacity influenced by dust grain growth, vertical settling, and radial drift, which control how deeply UV photons can penetrate into the gas disk (B. Jonkheid et al. 2007; T. Henning et al. 2010; P. Cazzoletti et al. 2018; J. K. Calahan et al. 2023). While the primary goal of this Letter is to report the detection of planet-driven HCN and C_2H intensity signatures in HD 163296, it is first necessary to characterize the radial and vertical emission structure of the host CSD in order to provide a robust estimate of the three-dimensional location of these signals relative to the background substructures.

As illustrated in the top panel of Figure 3, our best-fit model is in agreement with a HCN emission surface originating from intermediate layers at $z/R \approx 0.15-0.2$ above the disk midplane, closely matching the emission region of ^{13}CO $J = 2 \rightarrow 1$ (A. F. Izquierdo et al. 2023). This contrasts with the other four disks in the MAPS sample, where the bulk of the HCN emission appears to originate from midplane layers ($z/R < 0.1$) despite differences in stellar type and gas temperature (see T. Paneque-Carreño et al. 2023 for an analysis of the full sample). Such a distinction may indicate lower dust-to-gas mass ratios in those systems, allowing UV photons to penetrate more deeply and thereby push HCN emission to lower altitudes compared to HD 163296 (J. K. Calahan et al. 2023). We further analyzed the HCN emission surface using an independent, nonparametric method with the DISKSURF package (C. Pinte et al. 2018a; R. Teague et al. 2021), aiming to capture radial modulations in the HCN vertical distribution. This analysis confirms that emission from this tracer arises from layers at $z/R \approx 0.15-0.2$, except for the dips at 67 and 135 au, where the emission surface shifts to altitudes much closer to the midplane ($z/R < 0.1$).

Radially, the HCN intensity profile shows strong modulations within the region where dust substructures are most prominent at millimeter wavelengths ($R < 160$ au) and extends smoothly beyond this area, suggesting that UV-driven or gas-phase chemistry remains active in the cold outer disk (V. V. Guzmán et al. 2021). To characterize the HCN radial intensity distribution, we fixed all baseline model parameters—derived under the assumption of smooth intensity and Keplerian rotation—and introduced a second modeling step in which two Gaussian components were fitted to better reproduce the channel-by-channel emission of the disk.

This refined modeling reveals narrow HCN intensity rings centered at 47.6 and 114.3 au, with Gaussian widths (before convolution) of 2.5 and 7.3 au, respectively. At 79 au lies a prominent intensity dip, with peak brightness temperatures as low as 5 K, comparable to the low intensities observed in the outer disk (see Figure 3, bottom panel). Caution is warranted, however, within the inner ~40 au, where the continuum emission is strong (>20 K) and HCN is potentially optically thick (J. B. Bergner et al. 2021). In this region, continuum subtraction likely leads to an underestimation of the HCN intensity (see, e.g., Y. Boehler et al. 2017), suggesting that the HCN ring at 47.6 au may in fact extend further inward into the inner disk. Nevertheless, intensity modulations beyond this region appear robust. Using non-continuum-subtracted images, we confirm that the subsequent HCN substructures are present at the same locations, with the corresponding dip (81 au) and peak (103 au) lying within one beamwidth of the continuum-subtracted values. This is consistent with the findings of C. J. Law et al. (2021a), who reported no clear correlation

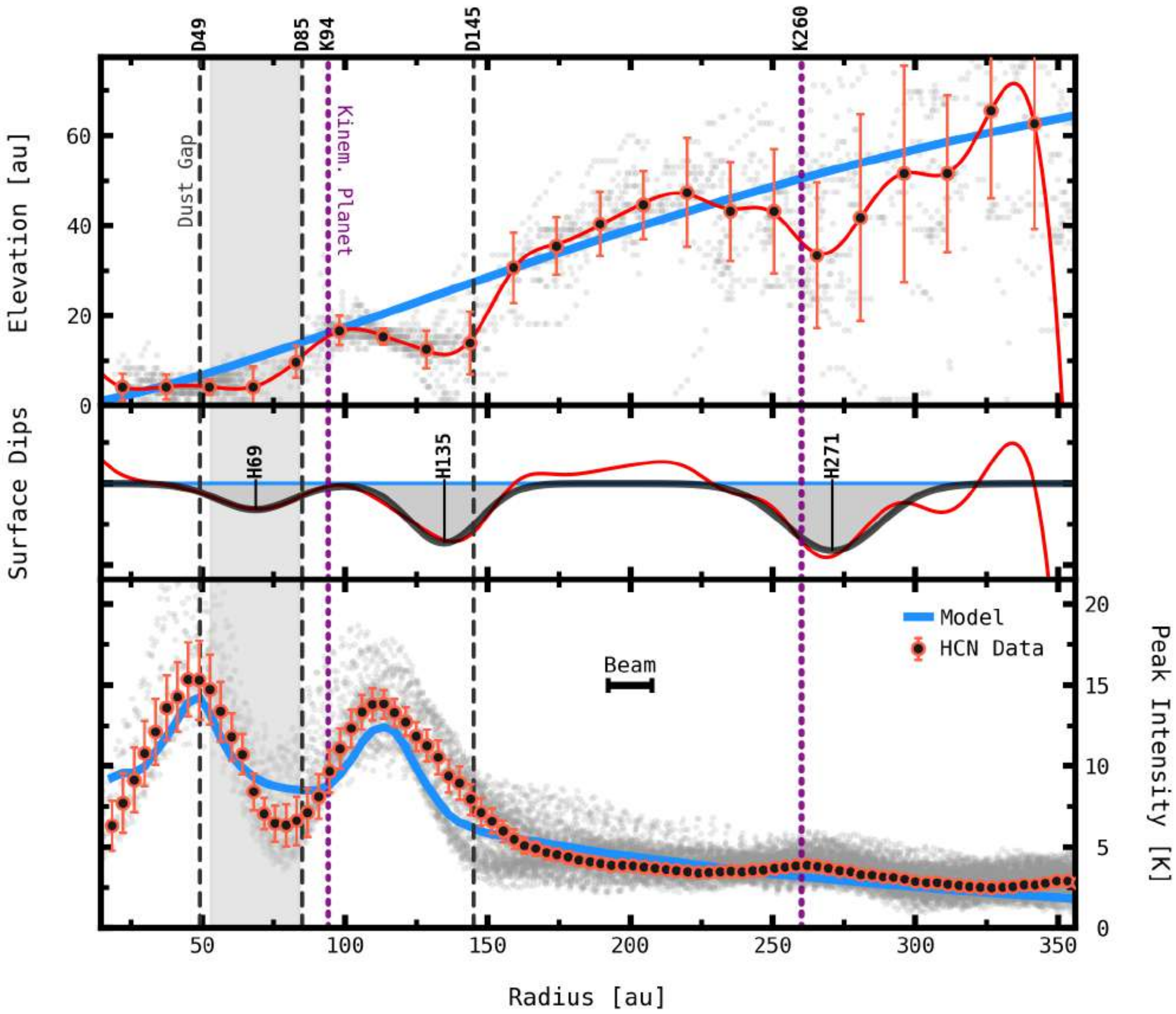

Figure 3. Elevation (top and middle) and peak intensity (bottom) profiles for the front side of the disk of HD 163296, probed by HCN ($J = 3-2$) emission, shown for both the best-fit model (blue curves) and the datacube (orange points). The DXX dashed lines mark the locations of the Band 6 dust gaps, while K94 and K260 indicate the orbital separations of previously reported kinematic planet candidates. The surface points in the top panel, extracted with DISKSURF, reveal significant vertical substructure, including two prominent 30 au wide dips at 69 and 135 au and a tentative dip at 271 au, labeled as HXX in the middle panel. An optically thin window, highlighted with gray shading and centered on the H69 dip, provides a view of the disk midplane near D85, where a localized signal associated with the P94 planet arises (see Section 3.2). The gray points in the bottom panel are peak intensity values mapped into the disk frame using the model's best-fit geometrical parameters.

between chemical and dust substructures across the MAPS sample of disks, suggesting that continuum subtraction is unlikely to play a dominant role in shaping the observed chemical signatures.

Notably, the identified intensity modulations do not consistently correlate with emission surface highs and lows or with the locations of dust rings and gaps, indicating that UV exposure is likely not the sole driver of HCN abundance in the disk; other key factors, such as temperature, the local C/O ratio, and the degree of disk flaring, may also play a significant role in shaping the molecule's distribution (see V. V. Guzmán et al. 2021, for a discussion).

3.2. Localized Intensity Signals in HCN and C_2H

A noteworthy feature of the HCN emission from the CSD is that the dip in surface height between the dust gaps D49 and D85, centered at 69 au, is also characterized by low optical depths as inferred from hyperfine structure analysis (J. B. Bergner et al. 2021). Combined with the system's moderate inclination, this property provides a unique window into regions near the disk midplane and enables a search for chemical signatures originating in the vicinity of any protoplanet potentially associated with the dust gap at 85 au, as illustrated in Figure 4. Indeed, within this zone, we detect localized intensity signals[9] that spatially coincide with previously reported ^{12}CO and ^{13}CO velocity perturbations linked to the Jupiter-mass candidate P94 (A. F. Izquierdo et al. 2022, 2023). We therefore attribute the origin of these signals to material surrounding the embedded protoplanet, possibly in the form of a CPD.

---

[9] The outermost regions of the CSD, beyond ~140 au, are also consistent with optically thin emission, but no localized signals stand out significantly in this area.

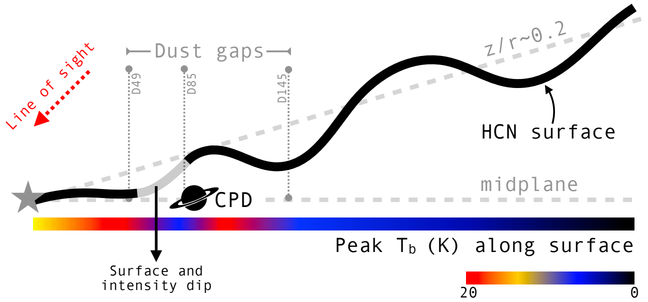

Figure 4. Cartoon illustrating the radial modulations in the disk surface traced by HCN emission and the relative location of the CPD candidate, whose emission is consistent with an origin near the midplane. This region is partially accessible thanks to a prominent HCN gap near the CPD's orbital separation and the moderate inclination of the disk.

The HCN chemical signatures around P94 are highlighted in Figure 5, and in Figure 7 of Appendix B for non-JvM-corrected and non-continuum-subtracted images. In Figures 8, 9, and 10 of Appendix B, these signals are further illustrated in channel maps of both HCN and C_2H emission. Crucially, although the HCN intensity signal from the CPD candidate is spatially localized, it is significant ($>5\sigma$) across multiple velocity channels and can therefore be robustly exploited for dynamical analysis. Some additional processing is required, however, as the signal is partially obscured by overlapping velocity components from the bright upper layers of the circumstellar disc along the line of sight.

The fact that the CPD signature is not entirely hidden by these upper layers can be explained by the expected vertical and radial offset between the CPD emission, assumed to originate near the disc midplane, and the surface height of the CSD intersecting the same line of sight. This offset produces an apparent spectral shift between the two components owing to differences in orbital velocity, allowing the CPD emission to remain visible in a subset of velocity channels (see Section 4.2 for a discussion of the vertical location of the proposed CPD signals).

To isolate the CPD emission and minimize contamination from the CSD, we leverage our knowledge of its three-dimensional structure (Section 2.2) and apply a folding technique in which spectra from the blueshifted side of the disk are subtracted from those on the redshifted side in the vicinity of the CPD. This procedure is illustrated in Figure 5, with the reconstructed CPD spectra shown in the bottom panel, extracted from a 7×7 pixel region (two beams per side) centered on the localized HCN signal. The brightest spectrum has a Gaussian amplitude of 5.9 mJy beam^{-1}, corresponding to a 7σ detection referred to the noise level of 0.8 mJy beam^{-1} in the same folded region, and a centroid velocity of 2.29 km s^{-1} measured relative to the systemic velocity of the CSD. Based on the 20% brightest spectra, we find a composite FWHM of 0.94 km s^{-1}, a median CPD orbital radius of $R = 88 \pm 7$ au, and an azimuth of $\phi = 46 \pm 3$ in the disk frame, corresponding to $R = 0\farcs75 \pm 0\farcs05$ and PA $= 350 \pm 3°$ in projected sky coordinates[10] (or $\Delta\alpha = -0\farcs13$, $\Delta\delta = 0\farcs74$), relative to the central star. This demonstrates a strong quantitative overlap between the proposed CPD and the kinematic planet P94 reported at $R = 94 \pm 6$ au, $\phi = 50 \pm 3$ by A. F. Izquierdo et al. (2022, 2023). Such an overlap is further supported by the fact that the radial location of planets inferred from localized velocity perturbations, such as P94, may be overestimated by 5%–10%, since this method appears to be slightly more sensitive to the outer planet-driven spiral wake than to the inner one, as demonstrated by previous modeling efforts (A. F. Izquierdo et al. 2021; J. Bae et al. 2025).

3.3. Dynamical Planet Mass and CPD Properties

Under the assumptions outlined later in this section, it is in principle possible to constrain some of the physical properties of the proposed CPD system, including the planet mass M_p, by noting that its line profile must be broadened by at least two components: the thermal motions of the gas, which contribute $\upsilon_{\rm th} = \sqrt{k_{\rm B}T/m_{\rm HCN}}$ to the intrinsic width of the line, and the orbital rotation of material around the planet, which induces velocity shifts in the bulk line profile but can effectively broaden it when the observations are unresolved. These effects are further modulated by the CPD radius $R_{\rm CPD}$ and inclination $i_{\rm CPD}$, which, together with the CPD temperature T, also determine the observed line intensity per velocity channel.

To combine these ingredients while accounting for the finite resolution of the observations, we generate DISCMINER channel-map models of the reconstructed CPD emission. Since the CPD signal is spatially unresolved, we implemented a subpixeling routine in our models to capture variations in the intensity and velocity gradients of the CPD, as detailed in Appendix A, in addition to the standard gridding at the native pixel scale and subsequent convolution by the beam. The compactness of the signal is consistent with theoretical expectations from angular momentum conservation, which implies that material slowly accreting into the Hill sphere of a forming planet is truncated at approximately one-third of the Hill radius (A. C. Quillen & D. E. Trilling 1998; B. A. Ayliffe & M. R. Bate 2009), defined as $R_{\rm Hill} = R_p(M_p/3M_\star)^{1/3}$. For a $1M_{\rm Jup}$ planet at 88 au, this yields a CPD radius of just ∼1.5 au—well below the ∼15 au beam size of the observations at the source distance. More recent 3D radiative hydrodynamic simulations have proposed slightly larger truncation scales, up to $\sim 0.6R_{\rm Hill}$ (J. Szulágyi 2017), yet still insufficient to be spatially resolved in the data.[11]

To reduce degeneracies among the key parameters of the CPD system that we aim to constrain (M_p, $R_{\rm CPD}$, and T), we assume that the CPD follows Keplerian rotation,[12] is geometrically thin, and is coplanar with the CSD (i.e., $i_{\rm CPD} = 46\overset{\circ}{.}7$). In addition, since the temperature of the CPD probed by HCN is currently unknown, we run nine separate models, each adopting a uniform gas temperature spanning values between $T = 25$ K and $T = 800$ K, with the thermal line broadening adjusted accordingly. The lowest temperature, 25 K, corresponds to the rotational temperature inferred by J. B. Bergner et al. (2021) for the CSD, based on analysis of the HCN hyperfine structure, at the orbital radius of the CPD candidate. The higher-temperature models are intended to

---

[10] The quoted uncertainties correspond to the standard deviation of the projected locations among the selected spectra.

[11] Even at this larger truncation radius, a prohibitively high companion mass of $15M_{\rm Jup}$ would be required for the emission to become spatially resolved.

[12] As discussed in Section 4.3, the strength and shape of the CPD's rotational component depend not only on the planet's mass but also, more generally, on its thermal history, which determines the relative contribution of pressure forces in supporting the gas around the planet. This complexity, however, lies beyond the scope of our simple parametric model, given the limitations imposed by the unresolved observations.

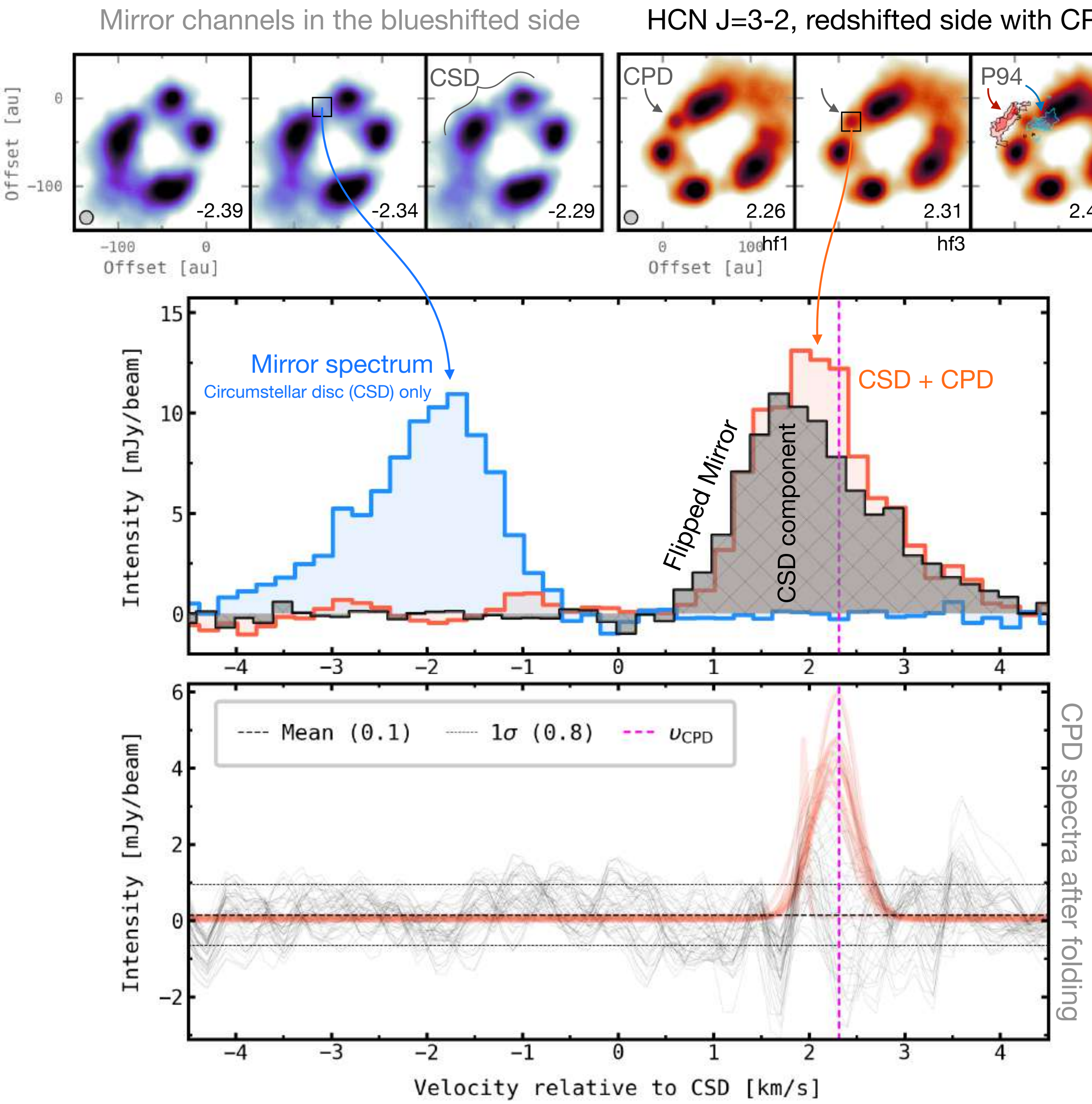

Figure 5. Illustration of the folding procedure used to isolate the HCN $J = 3$ 2 spectra from the localized signal around the kinematic planet P94, possibly tracing CPD emission. The blueshifted side of the CSD is spectrally mirrored and subtracted from the redshifted side, where the planet resides, retaining the excess intensity contribution from the candidate CPD. The bottom panel shows the resulting folded spectra extracted from a 7 × 7 pixel box (approximately two beams per side) centered on the proposed CPD location at $R = 0\farcs75$ and PA $= 350°$. Gaussian fits to the brightest 20% of the spectra are overlaid as orange lines. The global peak profile has an amplitude of 5.9 mJy beam^{-1} and a centroid velocity of 2.29 km s^{-1} marked by the vertical dashed line, measured with respect to the inferred systemic velocity of the CSD.

account for the planet's thermal/accretion heating, the CPD's internal viscous heating, and shock or compressional heating from infalling circumstellar material (J. Szulágyi et al. 2016; J. Szulágyi & C. Mordasini 2017; A. J. Cridland et al. 2025). Finally, we assume that the emission is optically thick, and thus the model peak intensity—prior to projection and convolution—is directly determined by the adopted temperature.

As a result, each model run includes six free parameters: planet mass M_p, central offsets x_p and y_p, centroid velocity $\upsilon_{\rm CPD}$ relative to the systemic velocity of the CSD, CPD position angle PA$_{\rm CPD}$, and CPD radius $R_{\rm CPD}$. After an initial burn-in phase of 5000 steps, we find that the Markov Chain Monte Carlo chains from all nine models have stabilized. The models were then run for an additional 15,000 steps to map the posterior distributions. Table 2 summarizes the median planet masses, CPD sizes, and systemic velocities, along with their associated uncertainties derived from the final 1000 steps of the parameter chains. Figure 11 in Appendix B illustrates the reconstructed CPD intensity channels, together with the corresponding model channel maps for the different adopted temperatures.

Table 2

Median Parameter Values and 16th and 84th Percentile Uncertainties Derived from the Marginalized Posterior Distributions (Final 1000 Steps) of the CPD Line Profile Models Introduced in Section 3.3, for Different Gas Temperatures

	25 K	50 K	75 K	100 K	150 K	200 K	400 K	600 K	800 K	Unit
M_p	$1.42^{+0.10}_{-0.12}$	$1.08^{+0.11}_{-0.11}$	$0.98^{+0.07}_{-0.08}$	$1.29^{+1.59}_{-0.23}$	$1.12^{+0.27}_{-0.34}$	$0.65^{+0.22}_{-0.22}$	$0.21^{+0.10}_{-0.06}$	$0.09^{+0.07}_{-0.06}$	$0.04^{+0.05}_{-0.03}$	$M_{\rm Jup}$
$R_{\rm CPD}$	$7.45^{+0.10}_{-0.09}$	$4.49^{+0.06}_{-0.10}$	$3.33^{+0.07}_{-0.07}$	$2.87^{+0.09}_{-0.15}$	$2.10^{+0.08}_{-0.05}$	$1.68^{+0.05}_{-0.08}$	$1.02^{+0.04}_{-0.04}$	$0.79^{+0.05}_{-0.04}$	$0.64^{+0.05}_{-0.05}$	au
$v_{\rm CPD}$	$2.26^{+0.01}_{-0.01}$	$2.26^{+0.02}_{-0.04}$	$2.26^{+0.01}_{-0.02}$	$2.31^{+0.19}_{-0.03}$	$2.32^{+0.03}_{-0.03}$	$2.31^{+0.02}_{-0.02}$	$2.31^{+0.02}_{-0.02}$	$2.35^{+0.02}_{-0.02}$	$2.38^{+0.02}_{-0.02}$	km s^{-1}

Note. The CPD centroid velocity, $v_{\rm CPD}$, is reported relative to the systemic velocity of the CSD, 5.79 km s^{-1}.

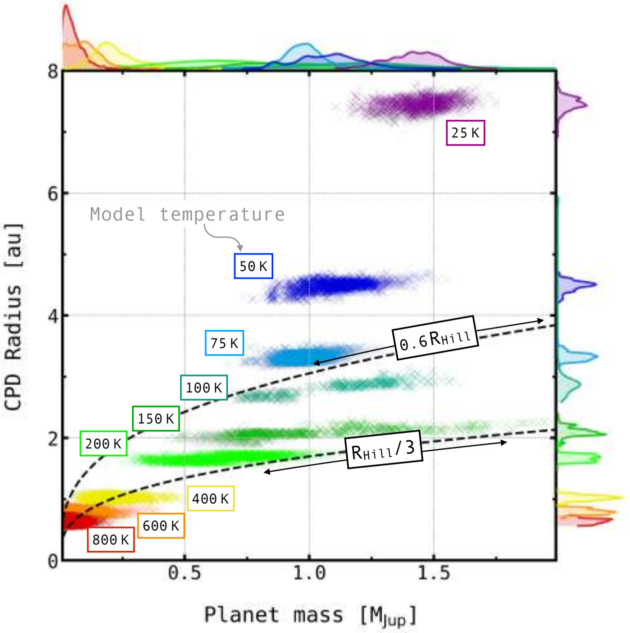

Figure 6. CPD radii and planet masses from the posterior distributions derived from our channel-map models of the localized HCN signal around the planet candidate P94. Model temperatures above 150 K yield CPD sizes consistent with theoretical expectations in which the CPD radius corresponds to roughly one-third of the planet's Hill radius.

The highest possible planet masses and CPD sizes are set by the coldest models at $T = 25$ K, which yield planet masses consistently below $1.8 M_{\rm Jup}$ and CPD radii no larger than 8 au. These two properties are compared across all models in Figure 6, which shows the posterior distributions relating CPD radius and inferred planet mass for each assumed temperature. Notably, the modeled planet mass range is broadly consistent—within a factor of two—with the previous estimate of $1 M_{\rm Jup}$ derived from analyses of surface density and velocity perturbations at the same location in the CSD (R. Teague et al. 2018a; A. F. Izquierdo et al. 2022).

More generally, we highlight that models with CPD gas temperatures of $T > 150$ K, planet masses $M_p < 1.0 M_{\rm Jup}$, and CPD radii $R_{\rm CPD} < 2$ au are most consistent with theoretical expectations in which the CPD outer boundary corresponds to approximately one-third of the planet's Hill radius. Considering the possibility of larger truncation scales $\sim 0.6 R_{\rm Hill}$ suggested by 3D radiative hydrodynamical simulations (e.g., J. Szulágyi 2017), these limits are relaxed by roughly 50%, yielding $T > 100$ K, $R_{\rm CPD} < 3$ au, and $M_p < 1.5 M_{\rm Jup}$. At the high end of the adopted temperature range, our models best reproduce the data for $T < 400$ K under our simplified assumptions of a uniform CPD temperature and Keplerian rotation. As illustrated in Figure 11, model temperatures above this threshold tend to flatten the line profile and overestimate the flux in the line wings. Nevertheless, the generally high temperatures favored by our models are in excellent agreement with a substantial increase in HCN abundance predicted by thermochemical models, where chemical reactions leading to HCN formation can overcome their activation barrier at a few hundred kelvin (see S. D. Doty et al. 2002 and Section 4.1 for a discussion), potentially explaining the origin of the detected signal.

Furthermore, the relatively low planet masses inferred from our analysis are consistent with the absence of hydrogen recombination lines (commonly used as tracers of ongoing accretion) in SPHERE/ZIMPOL data (N. Huélamo et al. 2022) and the lack of significant infrared emission in JWST/NIRCam observations of HD 163296 planet candidates, including P94 (T. Uyama et al. 2025). Indeed, theory indicates that extinction from the CSD and CPD may strongly attenuate both intrinsic luminosity and recombination-line emission, such that only planets with masses on the order of $2 M_{\rm Jup}$ or higher can produce thermal and accretion signatures detectable with current optical and infrared facilities (E. Sanchis et al. 2020; J. Szulágyi & B. Ercolano 2020). As such, anomalies in the surrounding chemistry, like the ones presented here, remain among the most powerful methods for directly investigating the properties of deeply embedded planets and their vicinities.

On the other hand, we note that the model CPD sizes are all consistently smaller than the width of the millimeter dust gap D85 ($\sim$16 au wide; J. Huang et al. 2018) in which the CPD resides, consistent with planet–disk interaction simulations predicting that millimeter gap widths can extend up to $10 R_{\rm Hill}$ (e.g., G. P. Rosotti et al. 2016). This suggests that the abundance of millimeter-sized grains in the circumplanetary region may be reduced owing to the limited inflow of particles aerodynamically trapped by pressure maxima at the gap walls, likely by the influence of the same parent planet P94 (A. F. Izquierdo et al. 2023). As a consequence, the associated millimeter flux is suppressed, reducing the likelihood of direct detection in the millimeter continuum as predicted by O. Chrenko et al. (2025). In contrast, we note that this radial section of the disk is not fully depleted in gas, with multiple species still emitting prominently (e.g., CO, HCO$^+$, H_2CO, CS; C. J. Law et al. 2021a). This suggests that gaseous material can continue to flow through the gap either along the midplane or from the upper disk layers and accrete onto the CPD, potentially further enriching its chemical composition.

We emphasize that the planet masses and CPD radii derived from our models should be regarded as initial estimates rather than firm constraints. Our simplified modelling neglects additional sources of line broadening such as hydrodynamical turbulence, inflow of material onto the CPD, hyperfine blending, and opacity broadening, which would generally act to reduce the inferred planet masses if included. Conversely, as discussed in Section 4.3, the omission of pressure support within the CPD leads to an underestimation of the planet mass. Future thermochemical and hydrodynamic models constrained by the observed features will improve the accuracy of the inferred CPD properties.

4. Discussion

4.1. Origin of the Observed CPD Chemical Signatures

The localized HCN and C_2H intensity signatures that we attribute to circumplanetary material around P94 may provide compelling evidence for an evolved chemical environment, sustained by high C/O ratios that favor carbon-rich chemistry, together with enhanced UV flux (L. I. Cleeves et al. 2015; A. D. Bosman et al. 2021) potentially driven by ongoing accretion onto the protoplanet (Y. Aoyama et al. 2018, 2020). This has important implications for the composition of the nascent planet–satellite system, as it could ultimately trigger the gas-phase formation of more complex organics within the planet-forming zone (J. K. Calahan et al. 2023).

Along with enhanced exposure to a planet-driven UV field, we may also be witnessing the effects of local planetary heating, enabling reactions between H_2 and small organic radicals such as CN and C_2. These reactions can overcome their activation barriers at temperatures of a few hundred kelvin—consistent with a subset of our CPD models—producing HCN and C_2H via $CN+H_2$ $HCN+H$ and C_2+H_2 C_2H+H (W. M. Pitts et al. 1982; G. He et al. 1998; S. D. Doty et al. 2002; L.-P. Ju et al. 2006). Such a mechanism can lead to enhancements in HCN abundances of up to two orders of magnitude at temperatures above ∼200 K (e.g., A. M. S. Boonman et al. 2001, as measured in high-mass hot cores). Relatedly, as demonstrated by L. I. Cleeves et al. (2015), even at relatively low temperatures just above $T \sim 44$ K, planetary heating from a Jupiter-mass planet can locally trigger the thermal desorption of HCN that would otherwise remain frozen out in the cold disk midplane. This process can significantly enhance the column density of the tracer in the planet's vicinity and has therefore been regarded as a promising indicator of planet presence.

The temperatures required to activate either of these chemical pathways in the proposed CPD of P94 are consistent with our models that best match theoretical expectations for CPD sizes, which yield temperatures significantly higher ($T > 100$ K) than those predicted for the CSD at the same location ($T \sim 25$ K; C. J. Law et al. 2021b). This indicates that localized heating is indeed active and potentially influencing not only the CPD's dynamical structure (see Section 4.3) but also the chemistry and observability of its molecular reservoir.

A similar conclusion was reached by J. Bae et al. (2022) for a candidate CPD embedded in the outskirts of the disk around the T Tauri star AS 209, where CPD temperatures of at least 35 K (exceeding the 22 K of the background disk) were required to explain the observed localized ^{13}CO emission. Despite differences in stellar type, evolutionary stage of the host stars, and orbital separation, this shared characteristic suggests that heating processes within CPDs may enhance the likelihood of detecting planetary seedbeds on wide orbits where the temperature contrast between the CPD and the CSD is expected to be substantial. O. Chrenko et al. (2025) explored an analogous scenario using radiative hydrodynamic simulations of warm CO bubbles around a Jupiter-mass planet at 120 au from a solar-mass star, far enough for the bubble to stand out against the cold CSD background. Despite the use of a different tracer, the combined contributions of the planet-induced bubble and the CSD to the total line intensity appear strikingly similar to the signatures observed around P94 in HD 163296.

4.2. Vertical Location of the CPD Emission

Another piece of evidence supporting the planetary origin of the localized signals is that they appear to arise from the disk midplane, where planet formation is most likely to occur as a result of the enhanced concentration of solids driven by hydrodynamical and gravitational instabilities (e.g., A. N. Youdin & F. H. Shu 2002; X.-N. Bai & J. M. Stone 2010). This is evidenced by the fact that, at the proposed orbital separation of the planet, the estimated systemic velocity of the candidate CPD matches the expected Keplerian velocity at the midplane, indicating that the CPD emission originates below the elevated HCN layer of the CSD.

This is illustrated in Figure 8 (Appendix B), where the localized intensity signal intersects the Keplerian isovelocity contour corresponding to the CPD systemic velocity only when the emission is deprojected assuming a midplane origin. Conversely, a consistent deprojection of the CSD emission is achieved only when adopting the appropriate emission surface height of $z/r \sim 0.2$, as derived from DISCMINER or DISKSURF modeling in Section 3.1.

4.3. Circumplanetary Disk or Envelope? Implications from the Observed Rotational Velocity

Hydrodynamical simulations of circumplanetary material carried out by J. Fung et al. (2019) indicate that the degree of rotational support within the CPD generally evolves over the planet's thermal history, with a response that may strongly depend on the planet-to-star mass ratio. Specifically, the authors demonstrate that in the initial envelope stage, when the circumplanetary gas behaves adiabatically on timescales shorter than the cooling time, the rotational component is negligible, as the gas is largely supported by a steep radial pressure gradient. Over timescales longer than the cooling time, as the system evolves toward an isothermal state, the pressure support weakens and the rotational component increases, gradually flattening the circumplanetary material into a disklike structure. In this state, the rotation approaches Keplerian values in the inner regions but remains consistently sub-Keplerian in the outer regions owing to residual pressure support (see also E. J. Lee & E. Chiang 2015; G. A. L. Coleman et al. 2017; E. Lega et al. 2024, for additional discussions).

Assuming an early adiabatic scenario in which thermal broadening dominates the observed line width of the proposed CPD, we find that a temperature of 1150 K would be required to reproduce the composite FWHM of 0.94 km s^{-1} exhibited by the HCN signal, following $\upsilon_{\rm fwhm} \equiv 2.355\sqrt{k_{\rm B}T/m_{\rm HCN}}$. Although this simplified estimate does not account for the finite resolution of the observations, it is consistent with our finding that for gas temperatures $T > 800$ K the rotational contribution of the CPD becomes negligible (as M_p 0; see Section 3.3). This effect has far-reaching implications for the inference of planet masses based on circumplanetary line emission, as early-stage, adiabatically heated configurations would largely suppress the observable kinematic imprint of the planet on the surrounding gas velocities (see J. Szulágyi 2017, for a discussion).

On the other hand, depending on whether the planet formed through a cold-start core accretion or hot-start gravitational instability pathway, its effective temperature, and consequently its thermal feedback onto the CPD, may differ significantly over time, with direct consequences for their chemical observability. For example, spectral and photometric models of a 1 Myr old Jupiter-mass planet predict effective temperatures of ∼500 K for a cold-start formation and ∼800 K for a hot-start scenario (D. S. Spiegel & A. Burrows 2012), implying that the observable chemical anomalies discussed in Section 4.1 would respond differently under each scenario. We therefore anticipate that future independent estimates of the CPD temperature, derived from multiwavelength studies and coupled with thermochemical models tailored to this system, will place strong constraints not only on the CPD's evolutionary state but also on the planet's formation pathway.

5. Conclusions

We report the detection of localized emission from simple organic molecules, HCN and C_2H, spatially coincident with the Jupiter-mass planet P94—previously proposed to explain CO kinematic perturbations in the disk of HD 163296—and thus possibly arising from a CPD structure. Although the signal is partially obscured by the upper layers of the CSD, a folding analysis comparing the redshifted and blueshifted sides of the system enables an approximate reconstruction of the candidate CPD spectrum in HCN with a significance of 7σ. The detected feature is centered at an orbital radius of $R = 88 \quad 7$ au and an azimuth of $\phi = 46 \quad 3$ in the disk frame (or $R = 0''.75 \pm 0''.05$ and PA $= 350 \quad 3$ in projected sky coordinates).

From a first-order dynamical analysis of the CPD spectrum in HCN, we derive an upper limit on the planet mass of $1.8 M_{\rm Jup}$, consistent with previous estimates from kinematics, and a CPD radius not exceeding 8 au, under the assumption that the CPD is Keplerian and coplanar with the CSD. By comparing the CPD sizes obtained from our models with theoretical expectations where the CPD radius is roughly one-third of the planet's Hill radius, we favor CPD gas temperatures $T > 150$ K, planet masses $M_p < 1.0 M_{\rm Jup}$, and CPD radii $R_{\rm CPD} < 2$ au.

Our analysis provides the first dynamical constraints on the properties of a forming planet and direct evidence for the presence of organic molecules in its vicinity, potentially sustained by high temperatures and UV irradiation driven by ongoing accretion onto the protoplanet. This establishes chemical anomalies as a powerful avenue for detecting circumplanetary regions and constraining the properties of embedded planets and a promising alternative in cases where thermal infrared emission and accretion lines are weak owing to (i) low planet masses, provided that sufficient planetary heating can overcome molecular activation barriers and desorption temperatures, or (ii) strong extinction from circumstellar and circumplanetary material.

Acknowledgments

Support for A.F.I. was provided by NASA through NASA Hubble Fellowship grant No. HST-HF2-51532.001-A awarded by the Space Telescope Science Institute, which is operated by the Association of Universities for Research in Astronomy, Inc., for NASA, under contract NAS5-26555. E.F.v.D. acknowledges support from the ERC grant 101019751 MOLDISK. M.B. and J.S. have received funding from the European Research Council (ERC) under the European Union's Horizon 2020 research and innovation program (PROTOPLANETS, grant agreement No. 101002188). This Letter makes use of the following ALMA data: ADS/JAO. ALMA#2018.1.01055.L. ALMA is a partnership of ESO (representing its member states), NSF (USA) and NINS (Japan), together with NRC (Canada), NSTC and ASIAA (Taiwan), and KASI (Republic of Korea), in cooperation with the Republic of Chile. The Joint ALMA Observatory is operated by ESO, AUI/NRAO and NAOJ. The National Radio Astronomy Observatory is a facility of the National Science Foundation operated under cooperative agreement by Associated Universities, Inc.

Software: ASTROPY (Astropy Collaboration et al. 2022), CASA (CASA Team et al. 2022), CMASHER (E. van der Velden 2020), DISCMINER (A. F. Izquierdo et al. 2021), DISKSURF (R. Teague et al. 2021), EMCEE (D. Foreman-Mackey et al. 2013), MATPLOTLIB (J. D. Hunter 2007), NUMPY (C. R. Harris et al. 2020), SCIKIT-IMAGE (S. van der Walt et al. 2014), SCIPY (P. Virtanen et al. 2020), RADIO-BEAM (E. Koch et al. 2021), SPECTRAL-CUBE (A. Ginsburg et al. 2019).

Appendix A

Modeling of Unresolved Velocity Gradients through Subpixeling

Because the CPD emission is localized, it is essential for the model to accurately capture variations in the assumed intensity, line width, and velocity parameterizations at unresolved scales before convolution. To achieve this, we implemented a subpixeling routine in DISCMINER, which enables a more accurate estimation of line profile properties on a pixel-by-pixel basis. Unlike the standard approach, at each step of the parameter search the peak intensity, width, and centroid velocity of the model lines are evaluated locally at the subpixel level. These values are then used to generate as many independent Gaussian line profiles as the number of subpixels, which are subsequently averaged to obtain the image pixel intensity for each velocity channel.

To resolve the CPD's radial extent by at least three elements, we adopt a grid of 11 subpixels per image pixel for models with temperatures $\leqslant 200$ K and 21 subpixels for those with temperatures >200 K, corresponding to effective resolutions of 0.4 and 0.2 au, respectively. We find that incorporating subpixeling can alter the amplitude and width of the resulting line profiles by up to 20% compared to the standard (non-subpixel) modeling.

Appendix B

Supporting Figures

Here we provide complementary figures that support the results presented in the main text. Figure 7 illustrates the isolated HCN $J = 3 \quad 2$ signal obtained from non-JvM-corrected and non-continuum-subtracted images, following the analysis described in Section 3.2. Figure 8 presents a deprojected view of one of the HCN channel maps containing emission from the CPD candidate, overlaid with the C_2H signal, highlighting the close alignment of the emission with the Keplerian isovelocity curve of the channel when the CPD

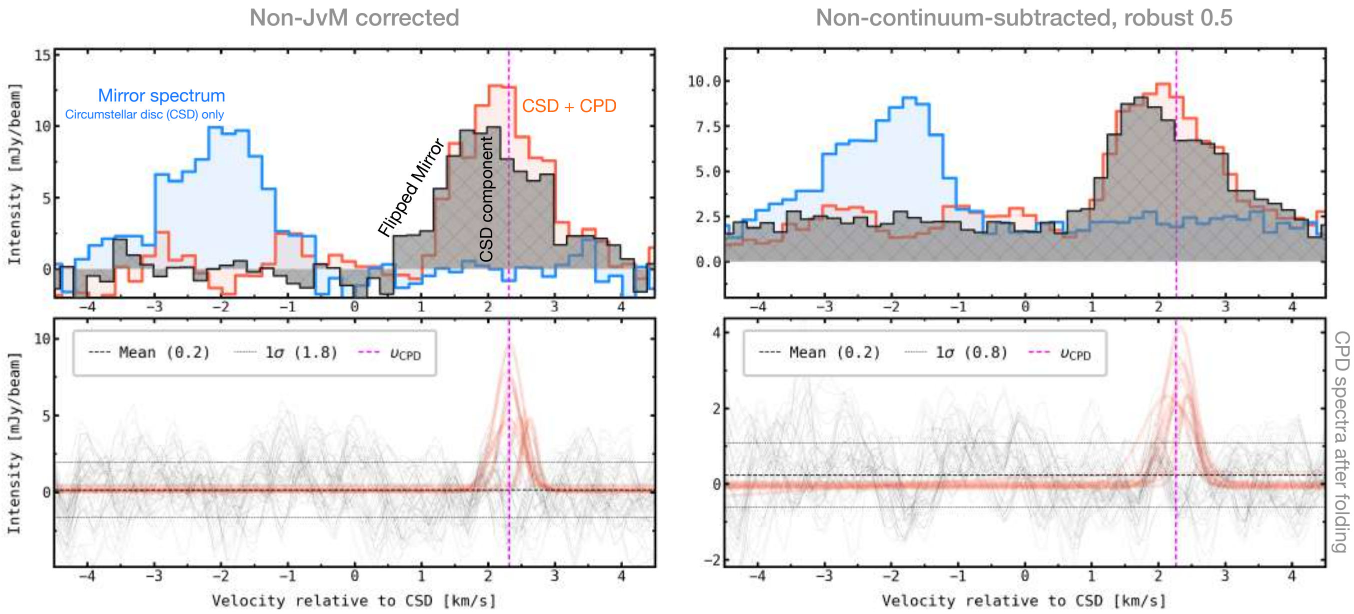

Figure 7. Same as Figure 5, but for JvM-uncorrected and non-continuum-subtracted data cubes.

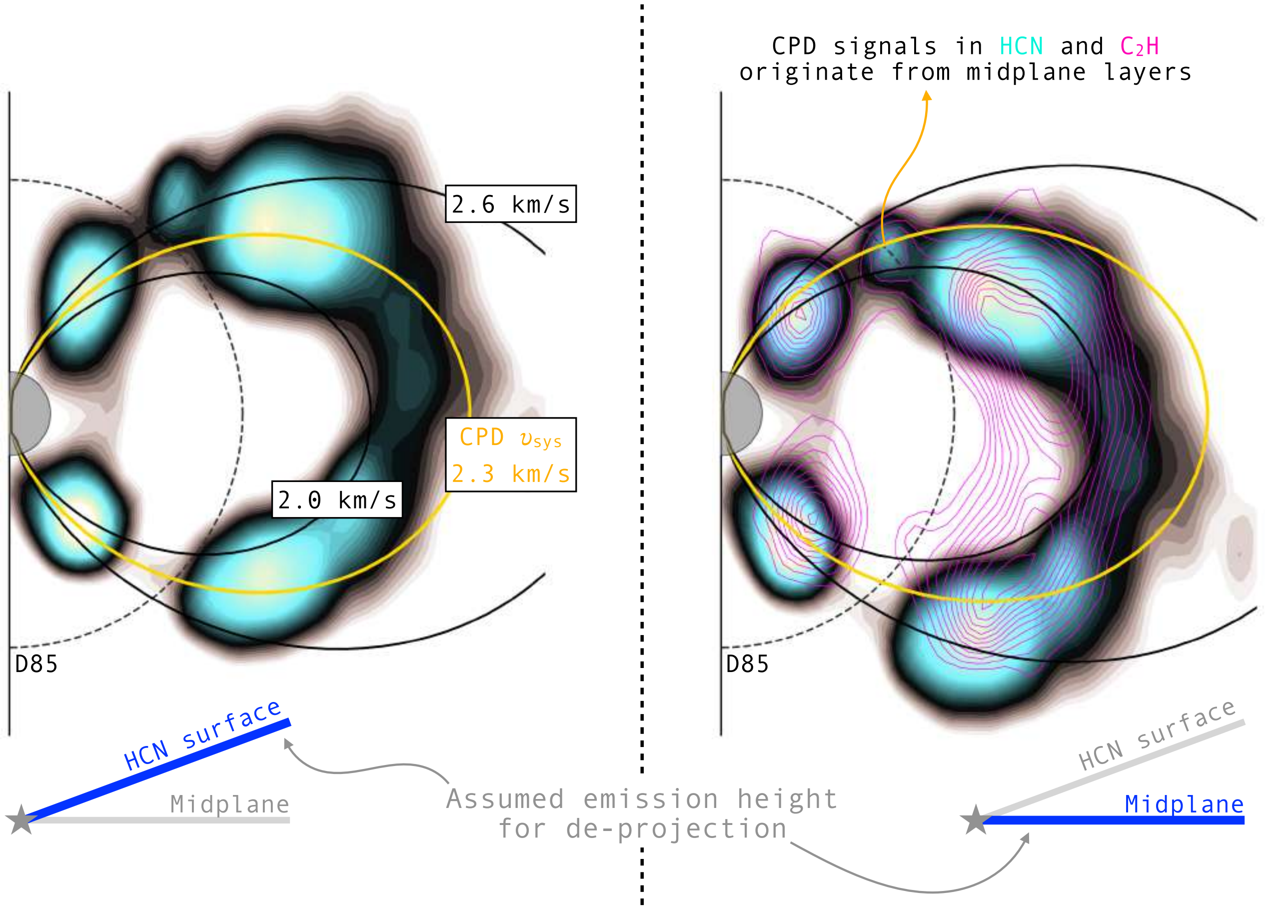

Figure 8. Deprojected view of the disk of HD 163296 as traced by HCN $J = 3 \rightarrow 2$ emission in the 2.3 km s^{-1} velocity channel relative to the CSD's $\upsilon_{\rm LSRK}$, assuming elevated (left panel) and midplane (right panel) emission heights. Overlaid are Keplerian isovelocity curves at values around the inferred CPD centroid velocity (∼2.3 km s^{-1}; see Section 3.3 for details). The observed CPD emission is consistent with a midplane origin, as indicated by its alignment with the isovelocity curve (yellow line) at the CPD centroid velocity when a $z/r = 0$ is adopted for the channel-map deprojection. The right panel also includes C$_2$H emission (in purple contours) at the same velocity channel, with the CPD signal overlapping that seen in HCN.

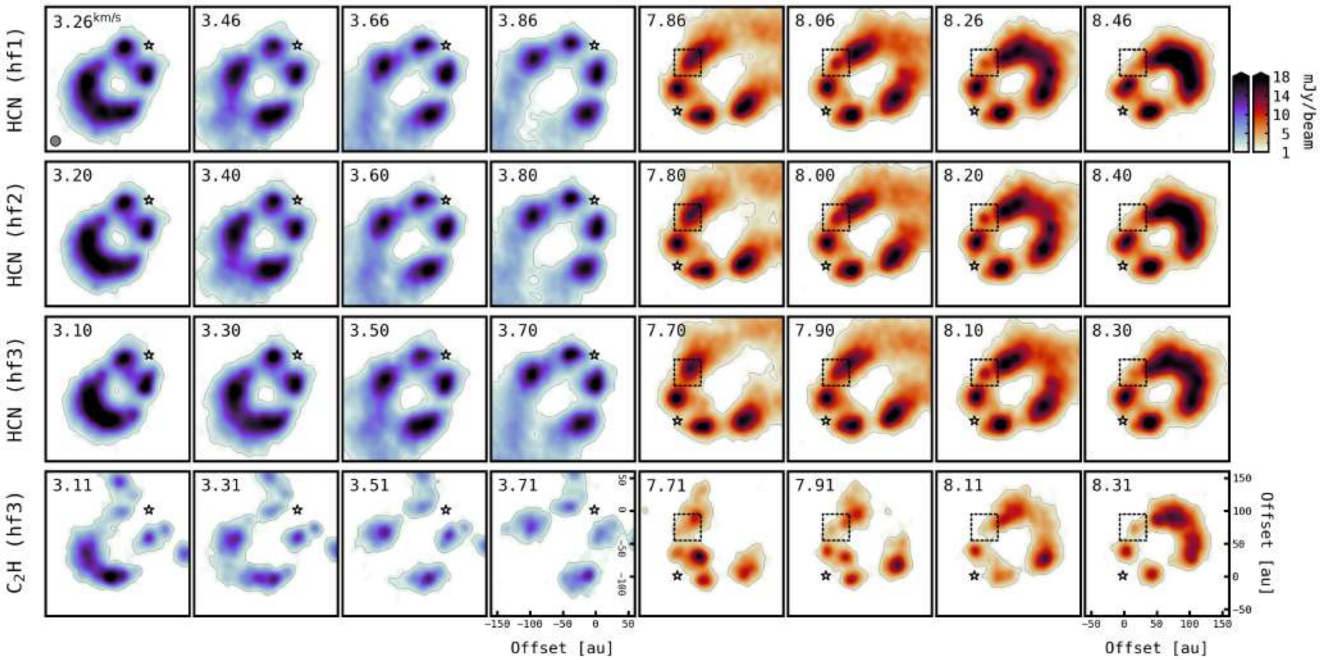

Figure 9. Selected intensity maps for HCN $J = 3 \rightarrow 2$ and C_2H $N = 3 \rightarrow 2$ $J = 5/2 \rightarrow 3/2$ $F = 3 \rightarrow 2$ lines, shown at mirrored (blue) and around (red) velocity channels where a localized signal overlaps with the kinematic planet candidate P94 first proposed by A. F. Izquierdo et al. (2022, 2023), providing unprecedented evidence of circumplanetary material orbiting a still-forming planet (see Section 3.3). A guiding dashed box is centered at the inferred location of the signal, at a projected separation of $R = 0\farcs75$ from the image center and a position angle of PA = 350°, measured from north through east. Although the HF1, HF2, and HF3 cubes for the HCN intensity channels correspond to datasets imaged at the central frequencies of different hyperfine components in the $J = 3 \rightarrow 2$ group, the bulk of the emission in all cases originates from the dominant $F = 4 \rightarrow 3$ line, blended with the $F = 2 \rightarrow 1$ and $F = 3 \rightarrow 2$ components. Contours enclose emission above five times the rms noise level of 0.43 mJy beam^{-1} for HCN and 0.53 mJy beam^{-1} for C_2H.

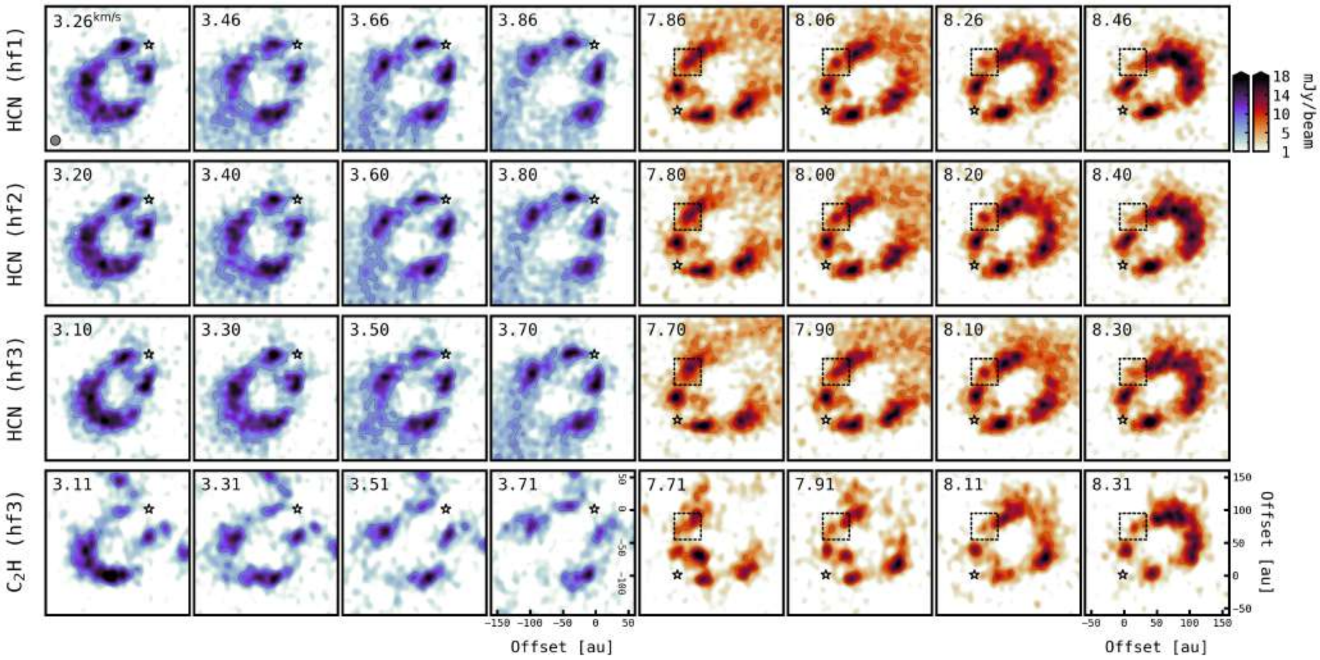

Figure 10. Same as Figure 9, but for JvM-uncorrected images. The rms noise levels are 1.38 mJy beam^{-1} for HCN and 1.61 mJy beam^{-1} for C_2H in these data cubes.

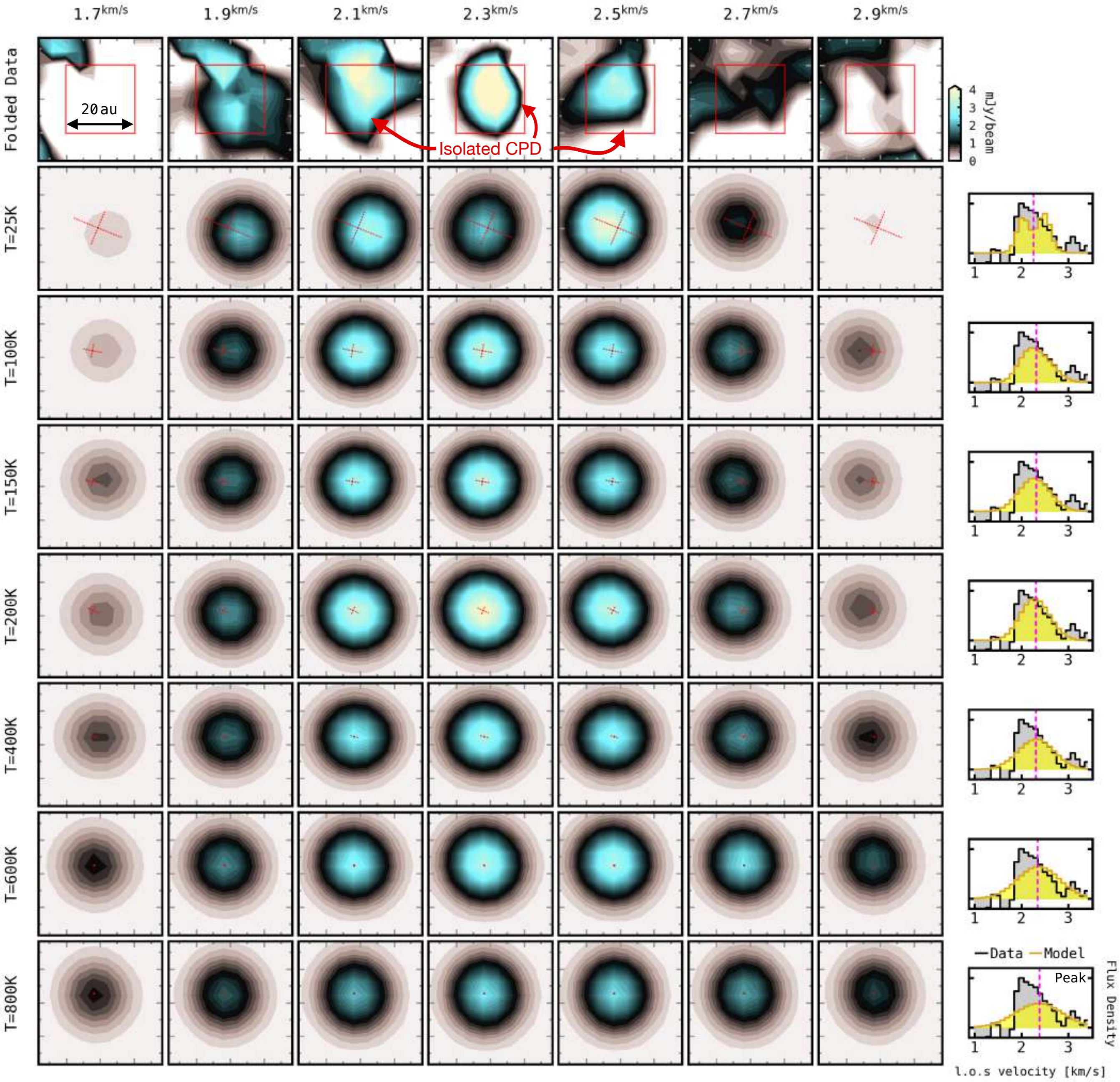

Figure 11. Folded HCN channel maps centered on the location of the P94 planet, with a field of view of two beam sizes, illustrating the isolated CPD signal (top row) and the corresponding best-fit models introduced in Section 3.3 for selected gas temperatures. The velocity channels indicated at the top are relative to the systemic velocity of the CSD, 5.79 km s^{-1}. The dotted lines overlaid on the model channels indicate the location and orientation of the projected CPD major and minor axes derived from the fit. The rightmost column shows a comparison between the flux density from the data (black) and the models (yellow), extracted from the red box shown in the top row and normalized to the peak data value of 4.66 mJy.

signal is assumed to originate near the disc midplane (see Section 4.2 for discussion). Figures 9 and 10 show HCN and C_2H channel maps around the detected signals for the JvM-corrected and non-JvM-corrected images, respectively. Finally, Figure 11 summarises the best-fit channel maps obtained in Section 3.3 for the HCN emission from the candidate CPD at selected model temperatures, together with a comparison of the corresponding flux-density profiles.

ORCID iDs

Andrés F. Izquierdo https://orcid.org/0000-0001-8446-3026
Jaehan Bae https://orcid.org/0000-0001-7258-770X
Maria Galloway-Sprietsma https://orcid.org/0000-0002-5503-5476
Ewine F. van Dishoeck https://orcid.org/0000-0001-7591-1907

Stefano Facchini https://orcid.org/0000-0003-4689-2684
Giovanni Rosotti https://orcid.org/0000-0003-4853-5736
Jochen Stadler https://orcid.org/0000-0002-0491-143X
Myriam Benisty https://orcid.org/0000-0002-7695-7605
Leonardo Testi https://orcid.org/0000-0003-1859-3070

References

Agúndez, M., Cernicharo, J., & Goicoechea, J. R. 2008, A&A, 483, 831
Agúndez, M., Roueff, E., Le Petit, F., & Le Bourlot, J. 2018, A&A, 616, A19
Andrews, S. M., Huang, J., Pérez, L. M., et al. 2018, ApJL, 869, L41
Aoyama, Y., Ikoma, M., & Tanigawa, T. 2018, ApJ, 866, 84
Aoyama, Y., Marleau, G.-D., Mordasini, C., & Ikoma, M. 2020, arXiv:2011.06608
Astropy Collaboration, Price-Whelan, A. M., Lim, P. L., et al. 2022, ApJ, 935, 167
Ayliffe, B. A., & Bate, M. R. 2009, MNRAS, 397, 657
Bae, J., Flock, M., Izquierdo, A., et al. 2025, ApJL, 984, L12
Bae, J., Teague, R., Andrews, S. M., et al. 2022, ApJL, 934, L20
Bai, X.-N., & Stone, J. M. 2010, ApJ, 722, 1437
Bailer-Jones, C. A. L., Rybizki, J., Fouesneau, M., Mantelet, G., & Andrae, R. 2018, AJ, 156, 58
Barraza-Alfaro, M., Flock, M., & Henning, T. 2024, A&A, 683, A16
Benisty, M., Bae, J., Facchini, S., et al. 2021, ApJL, 916, L2
Bergner, J. B., Öberg, K. I., Guzmán, V. V., et al. 2021, ApJS, 257, 11
Boehler, Y., Weaver, E., Isella, A., et al. 2017, ApJ, 840, 60
Boonman, A. M. S., Stark, R., van der Tak, F. F. S., et al. 2001, ApJL, 553, L63
Booth, A. S., Ilee, J. D., Walsh, C., et al. 2023, A&A, 669, A53
Bosman, A. D., Alarcón, F., Bergin, E. A., et al. 2021, ApJS, 257, 7
Calahan, J. K., Bergin, E. A., Bosman, A. D., et al. 2023, NatAs, 7, 49
Calcino, J., Hilder, T., Price, D. J., et al. 2022, ApJL, 929, L25
Canup, R. M., & Ward, W. R. 2002, AJ, 124, 3404
CASA Team, Bean, B., Bhatnagar, S., et al. 2022, PASP, 134, 114501
Cazzoletti, P., van Dishoeck, E. F., Visser, R., Facchini, S., & Bruderer, S. 2018, A&A, 609, A93
Chrenko, O., Casassus, S., & Chametla, R. O. 2025, A&A, 700, 82
Cleeves, L. I., Bergin, E. A., & Harries, T. J. 2015, ApJ, 807, 2
Cleeves, L. I., Öberg, K. I., Wilner, D. J., et al. 2018, ApJ, 865, 155
Coleman, G. A. L., Papaloizou, J. C. B., & Nelson, R. P. 2017, MNRAS, 470, 3206
Cridland, A. J., Lega, E., & Benisty, M. 2025, A&A, 693, A86
Czekala, I., Loomis, R. A., Teague, R., et al. 2021, ApJS, 257, 2
de Gregorio-Monsalvo, I., Ménard, F., Dent, W., et al. 2013, A&A, 557, A133
Doty, S. D., van Dishoeck, E. F., van der Tak, F. F. S., & Boonman, A. M. S. 2002, A&A, 389, 446
Foreman-Mackey, D., Hogg, D. W., Lang, D., & Goodman, J. 2013, PASP, 125, 306
Fung, J., Zhu, Z., & Chiang, E. 2019, ApJ, 887, 152
Ginsburg, A., Koch, E., Robitaille, T., et al. 2019, radio-astro-tools/spectral-cube: Release v0.4.5, Zenodo,doi:10.5281/zenodo.3558614
Guzmán, V. V., Bergner, J. B., Law, C. J., et al. 2021, ApJS, 257, 6
Harris, C. R., Millman, K. J., van der Walt, S. J., et al. 2020, Natur, 585, 357
He, G., Tokue, I., & Macdonald, R. G. 1998, JPCA, 102, 4585
Henning, T., Semenov, D., Guilloteau, S., et al. 2010, ApJ, 714, 1511
Huang, J., Andrews, S. M., Dullemond, C. P., et al. 2018, ApJL, 869, L42
Huélamo, N., Chauvin, G., Mendigutía, I., et al. 2022, A&A, 668, A138
Hunter, J. D. 2007, CSE, 9, 90
Isella, A., Benisty, M., Teague, R., et al. 2019, ApJL, 879, L25
Isella, A., Guidi, G., Testi, L., et al. 2016, PhRvL, 117, 251101
Isella, A., Huang, J., Andrews, S. M., et al. 2018, ApJL, 869, L49
Izquierdo, A. F., Facchini, S., Rosotti, G. P., van Dishoeck, E. F., & Testi, L. 2022, ApJ, 928, 2
Izquierdo, A. F., Testi, L., Facchini, S., et al. 2023, A&A, 674, A113
Izquierdo, A. F., Testi, L., Facchini, S., Rosotti, G. P., & van Dishoeck, E. F. 2021, A&A, 650, A179
Izquierdo, A. F., Stadler, J., Galloway-Sprietsma, M., et al. 2025, ApJL, 984, L8
Jonkheid, B., Dullemond, C. P., Hogerheijde, M. R., & van Dishoeck, E. F. 2007, A&A, 463, 203
Ju, L.-P., Han, K.-L., & Zhang, J. Z. H. 2006, JThCC, 05, 769
Koch, E., Ginsburg, A., AKL, et al. 2021, radio-astro-tools/radio-beam: v0.3.3, Zenodo, doi:10.5281/zenodo.4623788
Law, C. J., Booth, A. S., & Öberg, K. I. 2023, ApJL, 952, L19
Law, C. J., Loomis, R. A., Teague, R., et al. 2021a, ApJS, 257, 3
Law, C. J., Teague, R., Loomis, R. A., et al. 2021b, ApJS, 257, 4
Lee, E. J., & Chiang, E. 2015, ApJ, 811, 41
Lega, E., Benisty, M., Cridland, A., et al. 2024, A&A, 690, A183
Mesa, D., Langlois, M., Garufi, A., et al. 2019, MNRAS, 488, 37
Miki, S. 1982, PThP, 67, 1053
Miotello, A., Kamp, I., Birnstiel, T., Cleeves, L. C., & Kataoka, A. 2023, ASPC, 534, 501
Müller, H. S. P., Thorwirth, S., Roth, D. A., & Winnewisser, G. 2001, A&A, 370, L49
Mullins, A. M., Loughnane, R. M., Redman, M. P., et al. 2016, MNRAS, 459, 2882
Öberg, K. I., Facchini, S., & Anderson, D. E. 2023, ARA&A, 61, 287
Öberg, K. I., Guzmán, V. V., Walsh, C., et al. 2021, ApJS, 257, 1
Paneque-Carreño, T., Miotello, A., van Dishoeck, E. F., et al. 2023, A&A, 669, A126
Pinte, C., Ménard, F., Duchêne, G., et al. 2018a, A&A, 609, A47
Pinte, C., Price, D. J., Ménard, F., et al. 2018b, ApJL, 860, L13
Pitts, W. M., Pasternack, L., & McDonald, J. R. 1982, CP, 68, 417
Quillen, A. C., & Trilling, D. E. 1998, ApJ, 508, 707
Rabago, I., & Zhu, Z. 2021, MNRAS, 502, 5325
Rosotti, G. P., Juhasz, A., Booth, R. A., & Clarke, C. J. 2016, MNRAS, 459, 2790
Sanchis, E., Picogna, G., Ercolano, B., Testi, L., & Rosotti, G. 2020, MNRAS, 492, 3440
Spiegel, D. S., & Burrows, A. 2012, ApJ, 745, 174
Szulágyi, J. 2017, ApJ, 842, 103
Szulágyi, J., & Ercolano, B. 2020, ApJ, 902, 126
Szulágyi, J., Masset, F., Lega, E., et al. 2016, MNRAS, 460, 2853
Szulágyi, J., & Mordasini, C. 2017, MNRAS, 465, L64
Tanigawa, T., & Watanabe, S.-i. 2002, ApJ, 580, 506
Teague, R., Bae, J., Bergin, E. A., Birnstiel, T., & Foreman-Mackey, D. 2018a, ApJL, 860, L12
Teague, R., Bae, J., Birnstiel, T., & Bergin, E. A. 2018b, ApJ, 868, 113
Teague, R., Law, C. J., Huang, J., & Meng, F. 2021, JOSS, 6, 3827
Uyama, T., Ricci, L., Ygouf, M., et al. 2025, AJ, 169, 287
van der Velden, E. 2020, JOSS, 5, 2004
van der Walt, S., Schönberger, J. L., Nunez-Iglesias, J., et al. 2014, PeerJ, 2, e453
Virtanen, P., Gommers, R., Burovski, E., et al. 2020, scipy/scipy: SciPy v1.5.3, Zenodo, doi:10.5281/zenodo.4100507
Visser, R., Bruderer, S., Cazzoletti, P., et al. 2018, A&A, 615, A75
Walsh, C., Nomura, H., Millar, T. J., & Aikawa, Y. 2012, ApJ, 747, 114
Youdin, A. N., & Shu, F. H. 2002, ApJ, 580, 494
Zagaria, F., Jiang, H., Cataldi, G., et al. 2025, ApJ, 989, 30